ROYAL SOCIETY
OF CHEMISTRY

PAPER

Check for updates

Simultaneously achieving room-temperature circularly polarized luminescence and high stability in chiral perovskite nanocrystals *via* block copolymer micellar nanoreactors†

Minju Kim, [a] Jiweon Kim, [a] Jieun Bang, [a] Yu Jin Jang, [b] JaeHong Park [ac] and Dong Ha Kim *[acd]

Chiral hybrid halide perovskites have emerged as promising candidates for next-generation optoelectronic and spintronic devices owing to their outstanding chiroptical and electrical properties. However, designing chiral perovskite nanocrystals (NCs) that exhibit high stability as well as notable chiroptical activity under ambient conditions is still challenging. In this study, a novel strategy is developed to fabricate chiral perovskite NCs based on block copolymer inverse micelles with supramolecular chirality obtained by the self-assembly of optically inactive building blocks, polystyrene-*block*-poly(2-vinyl pyridine) (PS-*b*-P2VP) and DL-alanine (DL-ala). The selective occupation of perovskite precursors within chiral micellar cores ensures an efficient chirality transfer to the electronic states of the perovskite NCs, resulting in a high chiroptical response with an anisotropy factor of -2.0×10^{-4}, similar to those of the chiral ligand-modified perovskite NCs. Furthermore, circularly polarized luminescence performance is observed at room temperature. Simultaneously, the robust surface encapsulation by PS-*b*-P2VP/DL-ala inverse micelles protects the perovskite NCs from moisture, heat, and air more effectively than the pure PS-*b*-P2VP inverse micelles. This approach can be used to realize large-scale and low-cost production of chiral perovskites and can be extended to engineer chiral perovskite materials by judiciously controlling the block copolymer self-assembly.

10th anniversary statement

It is my greatest honor to contribute to the 10th anniversary issue with our recent findings on block-copolymer-driven hybrid chiral perovskite nanocrystals. I had precious chance to share our multidisciplinary studies on visible light-active photocatalysis mediated by strings of ZnO nanoparticles doped with carbon (2013), organic solar cells with P3PHT-*b*-P3HT surfactants (2016), ORR electrocatalysis using composite hollow nanostructures composed of carbon-coated Ti^{3+} self-doped TiO$_2$-reduced graphene oxide (2017), high-performance PtFe catalysts supported on electroactive Au-PANI core@shell nanoparticles (2017), water splitting *via* synergetic and antagonistic effects in the Ni- and Ru-based electrocatalysts (2019), and interfacial engineering of ZnO ETL by SAMs for perovskite solar cells (2020), and the most recent review on the development of anodes for Li–S batteries (2021), with the readers of this prestigious journal. It is my firm belief that the journal will grow as the flagship journal of the Royal Society of Chemistry as well as the representative materials-specific journal in the relevant scientific society. I can't wait to enjoy illuminating articles about innovative materials library designed for the challenges we face in artificial intelligence, 4G, human health, climate issue, *etc.* from the *Journal of Materials Chemistry A* as an author, reader, and editorial board member.

aDepartment of Chemistry and Nano Science, Division of Molecular and Life Sciences, College of Natural Sciences, Ewha Womans University, 52, Ewhayeodae-gil, Seodaemun-gu, Seoul 03760, Republic of Korea. E-mail: dhkim@ewha.ac.kr

bConvergence Research Center for Energy and Environmental Sciences, Sungkyunkwan University (SKKU), 2066 Seobu-ro, Jangan-gu, Suwon, Gyeonggi-do 16419, Republic of Korea

cNanobio Energy Materials Center (National Research Facilities and Equipment Center), Ewha Womans University, 52, Ewhayeodae-gil, Seodaemun-gu, Seoul 03760, Republic of Korea

dBasic Sciences Research Institute (Priority Research Institute), Ewha Womans University, 52, Ewhayeodae-gil, Seodaemun-gu, Seoul 03760, Republic of Korea

† Electronic supplementary information (ESI) available. See DOI: https://doi.org/10.1039/d2ta06996b

Introduction

Chiral hybrid halide perovskites have received tremendous attention in various applications, such as optoelectronic or spintronic devices, owing to their outstanding photophysical, optoelectronic, and chiroptical properties.[1,2] In particular, circularly polarized luminescence (CPL) emitted from chiral perovskites makes them available for a wide range of practical applications such as 3D displays,[3] anti-counterfeiting devices,[4] and CPL detectors.[5] In general, CPL-active chiral halide perovskites are synthesized by three approaches, including (1) the incorporation of chiral organic molecules as the A-site

cations,[5,6] (2) attachment of chiral ligands onto their surfaces,[7,8] and (3) chiral arrangement of achiral perovskite nanocrystals (NCs) using chiral materials.[9,10] However, due to significant nonradiative recombination, the CPL performance of chiral 2D perovskite mostly tends to be quenched at room temperature, with weak photoluminescence (PL) properties observed at room temperature. In addition, for the chiral perovskite NCs modified with chiral ligands,[8] the room temperature CPL is significantly reduced during the purification process, because the chiral ligands are easily detached from the surface. To address this problem, post-synthetic surface treatment using chiral ligands has been devised,[11,12] but the CPL properties were not clearly investigated. In the chiral assemblies of achiral perovskite NCs, high CPL performances are observed at room temperature. Still, additional optical elements which filter the unpolarized light emitted from perovskite NCs are required, limiting the affordability and solution processability. Therefore, there is an urgent need to design a new synthesis strategy for producing chiral perovskites with stable room temperature CPL performance and practical applicability.

Block copolymers (BCPs) have been recently used to fabricate well-ordered perovskite nanostructures owing to their ability to chemically interact with the perovskite and efficiently passivate the surface defects.[13] In particular, amphiphilic polystyrene-*block*-poly(2-vinyl pyridine) (PS-*b*-P2VP) served as a confined nanoreactor for the formation of perovskite NCs, allowing an easy control of the size and shape of the perovskite NCs, large-scale production, and improved environmental stability.[14–16] Recently, a new strategy to construct chiral helical polymer/perovskite hybrid nanofibers with CPL performance under ambient conditions and long-term stability was reported,[17] in which the CPL emission was induced by the handed-selective fluorescence absorption capacity of the chiral polymer matrix for the unpolarized light emitted from the perovskite NCs. In addition, a bilayer device composed of a perovskite polymer film and a chiral liquid crystal film was constructed to realize full-color CPL with a high asymmetry factor and improved environmental stability.[18] In both strategies, CPL activities originated from the helical supramolecular structure-induced chirality. The assembled achiral perovskite NCs were either confined in chiral host materials or combined with layered helical materials to form micron- or device-scale perovskite-based hybrid systems with CPL activity. However, the perovskite NCs themselves remain circular dichroism (CD) inactive, due to the lack of chemical interaction between them and the chiral host materials. In addition, to date, the development of a polymer template capable of imparting high stability and chirality to the perovskite has not yet been made. Inspired by this issue, we conjecture that chiral perovskite NCs can be crafted using chiral BCP inverse micellar nanoreactors that ensure an efficient chirality transfer as well as high stability. As higher chiroptical properties were observed in chiral 2D perovskites comprising a blend of chiral and achiral spacers and chiral perovskite nanoplates synthesized with a mixture of chiral and achiral ligands than those in their pure chiral counterparts,[19,20] it is believed that achiral molecules may contribute to chirality generation in perovskites. Nevertheless, there is still no research using an achiral platform with supramolecular chirality as a sole template to impart chirality into perovskites.
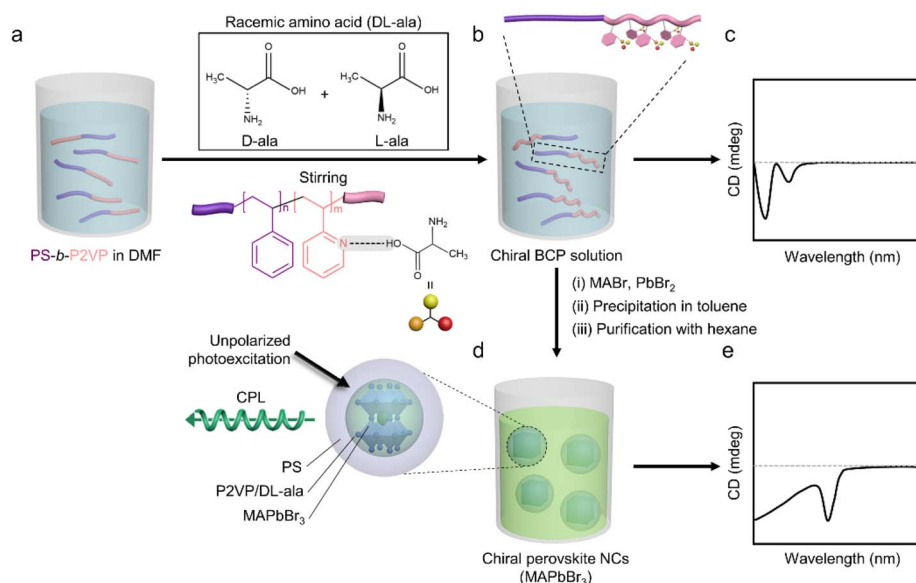
In this study, we devised a novel and facile route that utilizes BCP inverse micelles with supramolecular chirality induced by the self-assembly of achiral constituents for fabricating chiral perovskite NCs with stable CPL activity at room temperature and outstanding stability. We found that the hydrogen bonding between the achiral BCPs and racemic alanine induces the selective formation of polymeric nanoreactors with left-handedness. The strong coordination interactions between the chiral micellar cores and the perovskite precursors in the localized micellar environment enable an efficient chirality transfer, leading to the intrinsic chiroptical properties of the perovskite NCs characterized by negative CD and CPL signals under ambient conditions. In addition, long-term stability against harsh environments is achieved because the protective polymer shell effectively passivates the surface defects of the perovskite NCs crafted in the micellar core. Compared with the earlier methods for fabricating chiral perovskites, the present strategy provides a robust and viable platform that allows large-scale and low-cost manufacturing of chiral perovskites with the advantage of practical applicability in the ambient atmosphere.

Results and discussion

Fabrication of PS-*b*-P2VP/DL-ala inverse micelle-encapsulated MAPbBr$_3$ NCs

The synthesis route for chiral perovskite NCs based on achiral constituents is depicted in Fig. 1. First, an achiral PS-*b*-P2VP diblock copolymer dissolved in dimethylformamide (DMF) (Fig. 1a) is mixed with racemic DL-alanine (DL-ala), in which the carboxylic group of DL-ala can selectively bind to the polar P2VP block *via* the lone-pair electrons of the pyridine group (Fig. 1b). The supramolecular chirality of the BCP template is generated by the asymmetric polymer chain conformation induced by this noncovalent interaction,[21] as confirmed by the CD profile (Fig. 1c). Then, the added perovskite precursor salts (*i.e.*, MABr and PbBr$_2$) preferentially occupy the P2VP/DL-ala domain through a strong coordination with the amine groups of DL-ala. Finally, by dropwise addition of the solution into toluene, an antisolvent commonly used for perovskite precursors, the BCPs spontaneously form inverse micelles consisting of a P2VP/DL-ala core and a PS shell (Fig. 1d). Simultaneously, methylammonium lead bromide (MAPbBr$_3$) NCs are rapidly formed in the micellar cores, because the perovskite precursors undergo a supersaturation-induced recrystallization as they are transferred to the poor solvent.[22] To ensure a complete encapsulation of the perovskite NCs by the inverse micelle, further purification was performed using hexane, a poor solvent for both blocks, as a precipitant.[23,24] Because this purification step induces dense packing of the micelles onto the perovskite NCs and thus enhances the efficient chemical interactions in the confined micellar environment, chirality can be effectively transferred from the supramolecular structures to the perovskite NCs (Fig. 1e).

The supramolecular chirality of PS-*b*-P2VP induced by the complexation with alanine was investigated using CD
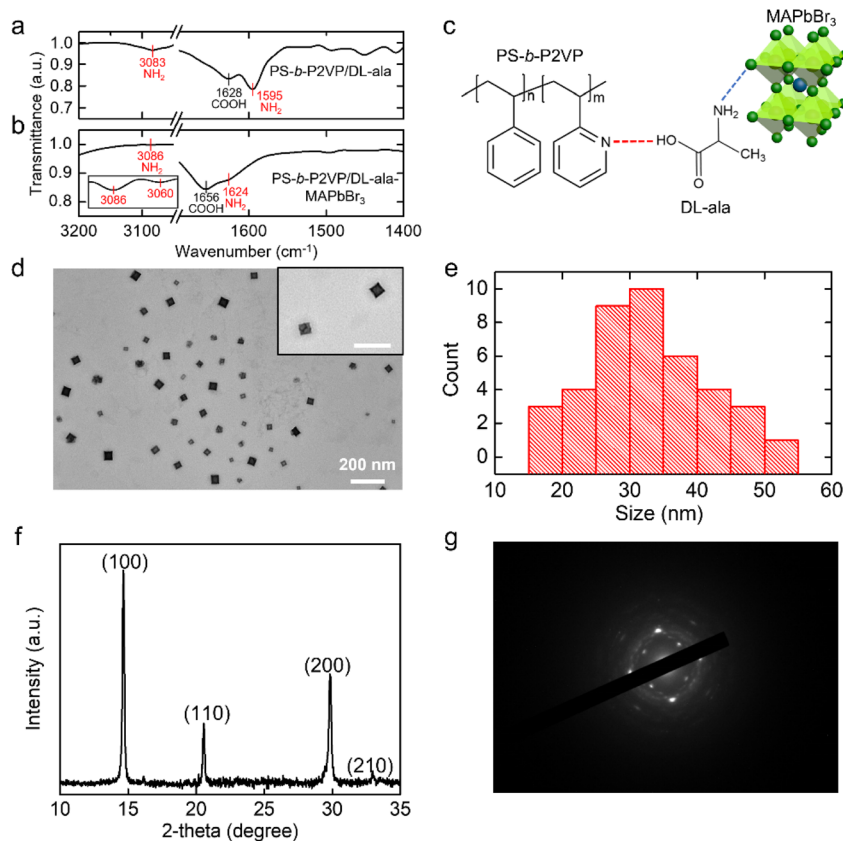
This journal is © The Royal Society of Chemistry 2023

J. Mater. Chem. A, 2023, **11**, 12876–12884 | **12877**

Fig. 1 Schematic illustration of the fabrication process of chiral perovskite NCs. (a) PS-b-P2VP is mixed with DL-ala in DMF to produce left-handed P2VP chains as shown in (b). The molecular structures of PS-b-P2VP and DL-ala are shown in the inset in (a). (b) Hydrogen bonding between the pyridine ring of P2VP and the carboxylic acid group of DL-ala leads to the formation of the helical P2VP chain with conformational chirality observed in (c). (d) Perovskite NCs are selectively grown within the micellar core after the addition of perovskite precursors, followed by precipitation and purification processes. The negative CD peak in (e) originated from the chirality transfer from polymer nanoreactors to perovskite NCs.

spectroscopy. The absorption and corresponding CD spectra of D-ala, L-ala, and DL-ala in aqueous solutions are provided in Fig. S1.† Mirror-image CD signals were detected at the n–π* transitions from L- and D-ala, whereas DL-ala produced no CD signal.[25] The pure PS-b-P2VP exhibited no CD response, confirming its achirality, whereas two negative cotton effects were observed at the n–π* and π–π* transitions of the pyridine for PS-b-P2VP mixed with L- or D-ala (Fig. S2†).[26] Interestingly, negative cotton effects arising from the left-handed helical conformation were observed,[27,28] irrespective of the molecular chirality of alanine, and the same CD behavior was also observed in PS-b-P2VP combined with DL-ala. To identify the origin of the supramolecular chirality, we mixed P2VP with L-, D-, and DL-ala, respectively. Similar to the result shown in Fig. S2,† two negative cotton effects appeared at the characteristic transition bands, irrespective of the kind of alanine enantiomers used (Fig. S3†). To confirm the non-covalent interactions between alanine and PS-b-P2VP, which are necessary for the evolution of supramolecular chirality, Fourier transform infrared (FTIR) spectroscopy was employed (Fig. S4†). In the FTIR spectra of pure alanine, the peak corresponding to the asymmetric –COOH stretching vibration was observed at 1625 cm⁻¹, which shifted to 1628 cm⁻¹ after complexation with PS-b-P2VP. The induced blue-shift is associated with the shortening of the –COO bond by hydrogen bonding.[29] In addition, the stretching vibration peak of pyridine at 1440 cm⁻¹ splits into two bands, 1459 and 1440 cm⁻¹, after complexation with alanine because of their hydrogen bonding interactions. This result agrees well with the previous literature, in which the stretching vibration peaks of pyridine for PS-b-P2VP split into

two bands because of the hydrogen bonding with the carboxylic acid group of tartaric acid.[30] The appearance of a new peak at a higher wavenumber is attributed to the restricted free rotation of the pyridine group by the hydrogen bonding.[31] Consequently, the hydrogen bonding between the carboxylic acid group of the alanine and the nitrogen of pyridine was clearly identified by the IR band shifts. This result suggests that the chemical interaction between alanine and the P2VP chain is the main driving force for the left-handed conformational change of P2VP, which determines the specific chirality of the BCP inverse micelles.

The role of the PS-b-P2VP/DL-ala inverse micelles as multidentate ligands was demonstrated via the FTIR spectroscopic analyses. As shown in Fig. 2a and b, the peak for the asymmetric –NH₂ bending vibration of DL-ala shifted from 1595 cm⁻¹ in PS-b-P2VP/DL-ala to 1624 cm⁻¹ in the PS-b-P2VP/DL-ala inverse micelle-encapsulated MAPbBr₃ NCs,[32] and that of the –NH₂ stretching vibration of the pure DL-ala at 3083 cm⁻¹ was split into two bands, as shown in the inset of Fig. 2b, in the hybrid composites. This peak shift and splitting may be attributed to the increased rigidity of the P2VP/DL-ala domains resulting from the preferential coordination of the perovskite precursors with the amine group of DL-ala.[33,34] Consequently, the carboxylic acid group of alanine participates in the hydrogen bonding with pyridine of the P2VP blocks, forming the P2VP/DL-ala cores, while the amine group of alanine becomes attached to the surface of the MAPbBr₃ NCs with a strong binding affinity for the halide ions (Fig. 2c). These chemical interactions play an important role in ensuring an effective encapsulation of the

12878 | J. Mater. Chem. A, 2023, **11**, 12876–12884

This journal is © The Royal Society of Chemistry 2023

Fig. 2 FTIR spectra of (a) PS-*b*-P2VP/DL-ala and (b) PS-*b*-P2VP/DL-ala inverse micelle-encapsulated MAPbBr$_3$ NCs. (c) Molecular structures showing the chemical interactions among PS-*b*-P2VP, DL-ala, and MAPbBr$_3$ NCs. (d) TEM image (inset: high-magnification TEM image, scale bar: 100 nm), (e) size distribution histogram (average size: 32.7 nm), (f) XRD pattern, and (g) the SAED pattern of the PS-*b*-P2VP/DL-ala inverse micelle-encapsulated MAPbBr$_3$ NCs.

perovskite NCs as well as efficient chirality transfer from the polymeric templates to the perovskite NCs.

Fig. 2d shows a transmission electron microscopy (TEM) image of the PS-*b*-P2VP/DL-ala inverse micelle-encapsulated MAPbBr$_3$ NCs with a cubic structure. Due to the high diffusion flow through rapid agitation and the reduced volume of the precursor solution, many small colloids were formed within a micelle core, which were then grown into single perovskite NCs by the Ostwald-ripening process.[14,35] The average size of the NCs was 32.7 nm with a relatively narrow size distribution (Fig. 2e). It was found that the addition of DL-ala evoked the formation of perovskite NCs (from 20 to 32.7 nm) with sizes that were larger than the average size of the PS-*b*-P2VP inverse micelle-encapsulated MAPbBr$_3$ NCs as seen in the TEM image (Fig. S5†). This effect of DL-ala on the structure of the perovskite NCs is associated with reduction in the number of trap defects,[36] which will be discussed later. To analyze the phase structures of the MAPbBr$_3$ NCs, X-ray diffraction (XRD) analysis was conducted. As evident from Fig. 2f, the XRD pattern was indexed to a well-defined cubic phase, where the characteristic diffraction peaks at 14.60°, 20.57°, 29.83°, and 32.95° can be assigned to the (100), (110), (200), and (210) planes, respectively.[37] The main diffraction peaks were observed at the same position for the PS-*b*-P2VP inverse micelle-encapsulated

MAPbBr$_3$ NCs (Fig. S6†). Additionally, as compared with Fig. S6,† the appearance of a strong and sharp diffraction peak corresponding to the (110) plane in Fig. 2f suggests that DL-ala can improve the crystallinity of MAPbBr$_3$ NCs. Furthermore, the selected-area electron diffraction (SAED) pattern showed the cubic crystal phase of the MAPbBr$_3$ NC (Fig. 2g),[38] which matched well with the XRD result. These results demonstrated that highly crystalline MAPbBr$_3$ NCs were successfully grown *in situ* within the PS-*b*-P2VP/DL-ala inverse micellar nanoreactor.

Investigation of chiroptical properties

The optical properties of the PS-*b*-P2VP/DL-ala inverse micelle-encapsulated MAPbBr$_3$ NCs were investigated by absorption and PL spectroscopy. Fig. 3a shows an absorption band with a band edge of approximately 515 nm and a sharp emission peak at 532 nm with a full width at half maximum of 20 nm. The prepared perovskite NCs exhibited a PL quantum yield (PLQY) of 30%, despite the fact that small amino acids can dynamically interact with perovskites, promoting charge transfer and inhibiting radiative recombination.[39,40] We then evaluated the chiroptical properties using CD and CPL spectroscopy under ambient conditions. The MAPbBr$_3$ NCs exhibited a strong negative CD signal near the absorption band, confirming that the chiral inverse micelle encapsulation endowed chiroptical
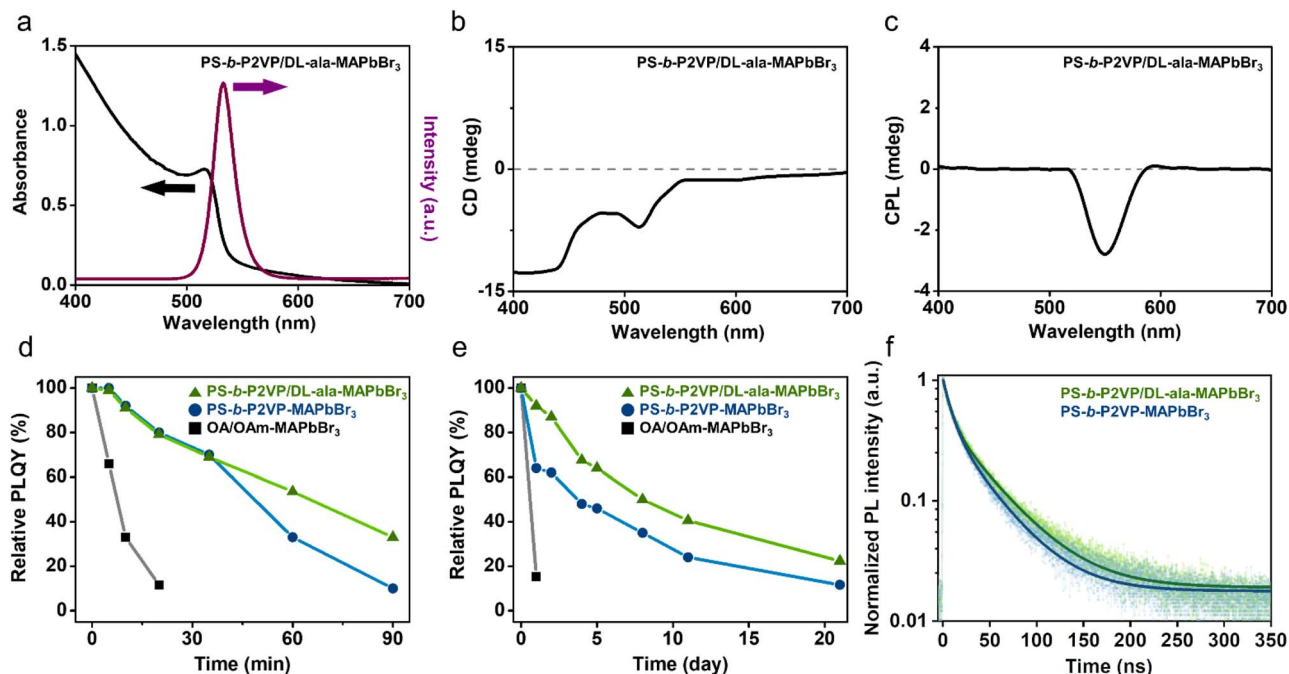
Fig. 3 Optical characterization and stability of the chiral perovskite NCs. (a) Absorption and PL spectra, (b) CD spectrum, and (c) CPL spectrum of the PS-*b*-P2VP/DL-ala inverse micelle-encapsulated MAPbBr$_3$ NCs. The PL and CPL measurements were performed at room temperature under excitation with a 365 nm unpolarized light. (d) Water and (e) thermal stabilities of the PS-*b*-P2VP/DL-ala inverse micelle-encapsulated MAPbBr$_3$ NCs (green). The OA/OAm-cocapped MAPbBr$_3$ NCs (black) and the PS-*b*-P2VP inverse micelle-encapsulated MAPbBr$_3$ NCs (blue) were used as controls. (f) TRPL decay profiles of PS-*b*-P2VP and PS-*b*-P2VP/DL-ala inverse micelle-encapsulated MAPbBr$_3$ NCs (blue and green, respectively) at 525 nm. The *y*-axis is plotted on a logarithmic scale, and the solid lines indicate the fitting results obtained using a biexponential decay equation. The purification was performed to ensure complete encapsulation of the MAPbBr$_3$ NCs by the inverse micelles.

properties into the inorganic Pb–Br framework *via* an efficient chirality transfer (Fig. 3b). The anisotropy factor was determined to be -2.0×10^{-4}, which is noticeably high, similar to those of the chiral octylamine-modified perovskite NCs,[7,8] even though the fabrication was carried out in the absence of chiral molecules to prepare the chiral templates. Furthermore, a negative CPL response was recorded at 550 nm under unpolarized photoexcitation at room temperature (Fig. 3c). Accordingly, it is concluded that the chiral perovskite NC was successfully crafted within the chiral polymeric nanoreactor, where the observed negative chiroptical properties are attributed to the strong interactions between the left-handed P2VP/DL-ala micellar cores and the perovskite NCs in the confined polymeric micellar environments.

We found that DL-ala played a crucial role in introducing chirality into the perovskite NCs. As a control experiment, we synthesized PS-*b*-P2VP inverse micelle-encapsulated MAPbBr$_3$ NCs without DL-ala. The perovskite precursors can selectively coordinate with the P2VP blocks because of the Lewis acid–base interactions between the lone pair of electrons on the N atoms of pyridine and the 6p vacant orbitals of Pb^{2+}.[15,34] Similar optical properties were observed, but no chiroptical properties were recorded at the characteristic optical band (Fig. S7 and S8†). We also synthesized PS-*b*-P2VP inverse micelle-encapsulated MAPbBr$_3$ NCs using chiral additives, L- and D-ala, instead of DL-ala. As shown in Fig. S9 and S10,† the replacement of DL-ala with either L- or D-ala did not alter the chiroptical properties and

anisotropy factors of the perovskite NCs. These results indicate that not the molecular chirality of alanine, but the supramolecular chirality generated by the co-assembly of the BCPs and DL-ala is the origin of the chirality evolution of the perovskite NCs. Moreover, we demonstrated that any type of alanine could be used as an additive for the synthesis of chiral perovskite NCs encapsulated by BCP inverse micelles. Remarkably, because the use of racemic alanine instead of alanine enantiomers can significantly lower the production cost of the chiral perovskite NCs,[41] this strategy can realize large-scale manufacturing of chiral perovskite NCs.

Stability test

To verify the role of the PS-*b*-P2VP/DL-ala inverse micelles as a protective shell, the stability of the PS-*b*-P2VP/DL-ala inverse micelle-encapsulated MAPbBr$_3$ NCs was evaluated in comparison with that of the PS-*b*-P2VP inverse micelle-encapsulated MAPbBr$_3$ NCs and oleic acid (OA)/oleylamine (OAm)-cocapped MAPbBr$_3$ NCs. Water stability was tested after injecting a drop of water (50 μL) into the sample (2 mL) under vigorous stirring to accelerate the degradation process.[42] For the OA/OAm-cocapped MAPbBr$_3$ NCs, the water easily penetrated and came into contact with the NCs, leading to a rapid PL intensity drop (Fig. 3d). In contrast, the polymeric inverse micelles effectively protected the NCs against water penetration, and as a result, the polymeric inverse micelle-encapsulated NCs displayed long-
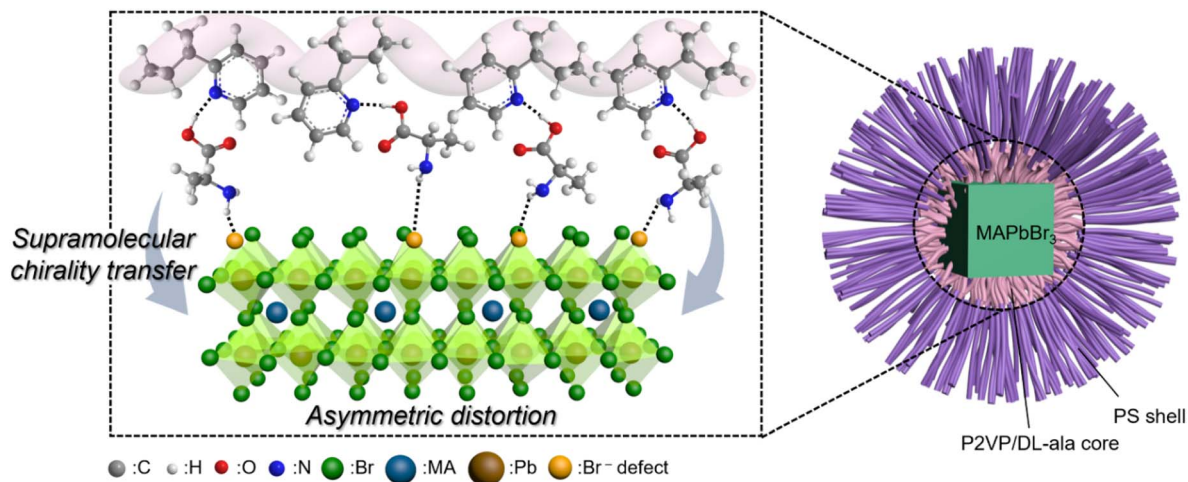
Fig. 4 Proposed mechanism for the origin of chirality in the PS-*b*-P2VP/DL-ala inverse micelle-encapsulated MAPbBr$_3$ NCs, illustrating that the P2VP/DL-ala chains passivating the NC surfaces cause asymmetric surface lattice distortions.

term water stability. We noted that the PS-*b*-P2VP/DL-ala inverse micelle-encapsulated MAPbBr$_3$ NCs retained a three-fold higher relative PLQY, compared to the inverse micelle-encapsulated NCs prepared in the absence of DL-ala after exposure to water for 90 min. Thermal stability was also assessed by heating the samples at 80 °C for up to 21 days (Fig. 3e). The short ligand-capped perovskite NCs suffered significant PLQY loss after 1 day, whereas the polymeric inverse micelle-encapsulated perovskite NCs retained PLQY even after 21 days. Interestingly, the PS-*b*-P2VP/DL-ala inverse micelle-encapsulated MAPbBr$_3$ NCs exhibited a two-fold higher relative PLQY, compared to the inverse micelle-encapsulated NCs without DL-ala, on the last day.

Time-resolved PL (TRPL) measurements were conducted to examine the surface passivation effect of the PS-*b*-P2VP/DL-ala inverse micelles on the perovskite NCs, in comparison with that of the pure inverse micelle and the OA/OAm ligand. The TRPL decay profiles, which were monitored at 525 nm and fitted with a biexponential decay function, showed fast time-constant components (τ_1) of 8.81 ($a_1 = 0.601$) and 7.84 ns ($a_1 = 0.583$), respectively and were followed by slow time-constant components (τ_2) of 38.6 ($a_2 = 0.399$) and 43.3 ns ($a_2 = 0.417$) for PS-*b*-P2VP and the PS-*b*-P2VP/DL-ala inverse micelle-encapsulated MAPbBr$_3$ NCs, respectively (Fig. 3f and Table S1†). The fast components are attributed to the trap-assisted charge recombination, whereas the slow components are correlated to the radiative recombination of the free carriers.[43–45] The lifetime-weighted average decay time (τ_{avg}) was determined using eqn (1):

$$\tau_{avg} = \frac{a_1\tau_1^2 + a_2\tau_2^2}{a_1\tau_1 + a_2\tau_2} \qquad (1)$$

The τ_{avg} of the prepared MAPbBr$_3$ NCs was 36.2 ns, which is 17% longer than that of the inverse micelle-encapsulated NCs prepared without DL-ala and much longer than the lifetime-weighted average decay time of the conventional oleate

ligand-capped MAPbBr$_3$ NCs (around 15.6 ns).[46] Furthermore, the addition of DL-ala into the micellar cores resulted in a reduced amplitude of the fast decay component (a_1: 0.601 *vs.* 0.583), implying that the trap defects on the NC surfaces were efficiently passivated by DL-ala.[36,47] Thus, we found that the P2VP/DL-ala cores enabled an effective passivation of the trap sites on the surface of the MAPbBr$_3$ NCs through strong coordination interactions.

To gain more insights into the effect of DL-ala on the stability, we also evaluated the water and thermal stabilities of PS-*b*-P2VP and the PS-*b*-P2VP/DL-ala inverse micelle-encapsulated MAPbBr$_3$ NCs prepared without the purification step (Fig. S11†). The PS-*b*-P2VP/DL-ala inverse micelle-encapsulated MAPbBr$_3$ NCs exhibited higher stabilities than those without DL-ala, demonstrating that the robust encapsulation occurred owing to the strong interactions between the P2VP/DL-ala cores and the perovskite NCs even in the absence of the further purification step.

Origin of chirality in perovskite NCs

Alanine can be incorporated into the perovskite framework as an organic cation or co-cation, or attached to the perovskite surface as a ligand.[48–50] To clarify the role of DL-ala in the evolution of chirality in the perovskite NCs, we fabricated (DL-ala)PbBr$_3$ NCs encapsulated by PS-*b*-P2VP inverse micelles and investigated their optical properties. Similar to previous work,[48] the onset of absorption was observed at 360 nm, but chirality was not detected (Fig. S12†), thus confirming that DL-ala serves as a surface ligand in this proposed system. It has been demonstrated that the chirality of the perovskite could be attributed to symmetry-breaking surface lattice distortions caused by the asymmetric interactions between the chiral surface ligands and the perovskite lead bromide octahedra.[51,52] Based on the aforementioned results and previously reported studies on the chiral origin, we established a plausible mechanism for the chirality evolution in the perovskite NCs (Fig. 4). Within the localized P2VP/DL-ala micellar core, the amine group

This journal is © The Royal Society of Chemistry 2023

J. Mater. Chem. A, 2023, **11**, 12876–12884 | **12881**

of DL-ala bonded with P2VP can effectively passivate the Br-rich defects on the perovskite NC surfaces through $[Br\cdots H-N^+]$ hydrogen-bonding interactions,[53] as revealed by the FTIR result (Fig. 2b). The asymmetric interactions between the left-handed P2VP/DL-ala and the perovskite NCs may induce distortions in the surface lattice, leading to a chirality transfer from the conformational chirality of the P2VP/DL-ala cores to the chirality of the NCs across the organic–inorganic interface. Therefore, negative chiroptical properties can be generated in the perovskite NCs.

Conclusions

We developed a simple and robust strategy for fabricating chiral MAPbBr$_3$ NCs based on chiral inverse micellar nanoreactors formed by the self-assembly of achiral BCPs and racemic mixture, DL-ala. We demonstrated that DL-ala plays a vital role as the simplest chiral source for inducing supramolecular chirality and imparting chirality in perovskite NCs through coordination interactions with the perovskites. The prepared chiral MAPbBr$_3$ NCs exhibited a strong negative CD signal with an anisotropy factor of -2.0×10^{-4}, comparable to those of the chiral octylamine-modified perovskite NCs, as well as a negative CPL signal at room temperature. The strong chiroptical properties were attributed to the efficient chirality transfer from the supramolecular structure in the localized micellar environment. In addition, the superior surface passivation by the P2VP/DL-ala micellar cores rendered the perovskite NCs highly resistant to moisture and temperature. This improvement was validated by the observed long-term stable optical properties of the inverse micelle-encapsulated perovskite NCs compared to those encapsulated by low-molecular-weight ligands and pure BCP inverse micelles. The proposed approach provides a novel supramolecular platform consisting of achiral building blocks for fabricating chiral perovskite NCs as well as ensures large-scale and low-cost production of chiral perovskite NCs for application in advanced chiral optoelectronic devices.

Experimental section

Materials

Polystyrene-*block*-poly(2-vinyl pyridine) (PS-*b*-P2VP, $M_{n,PS}$ = 172 kg mol^{-1}, $M_{n,P4VP}$ = 41 kg mol^{-1}) and poly(2-vinyl pyridine) (M_n = 8 kg mol^{-1}) were purchased from Polymer Source. Methylammonium bromide (MABr, 98%), lead(II) bromide (PdBr$_2$, 99.999% trace metals basis), toluene (anhydrous, 99.8%), D-alanine (≥98%), L-alanine (≥98%), oleic acid (OA, technical grade, 90%), oleylamine (OAm, technical grade, 70%), hydrobromic acid (HBr, ACS reagent, 48%), and *N*,*N*-dimethylformamide (DMF, anhydrous, 99.8%) were obtained from Sigma-Aldrich. DL-alanine (DL-ala, 99%) was purchased from Acros Organics. Isopropyl alcohol (99.7%), ethyl alcohol (anhydrous, 99.9%), and *n*-hexane (anhydrous, 99%) were purchased from Daejung.

Synthesis of the PS-*b*-P2VP/DL-ala inverse micelle-encapsulated MAPbBr$_3$ NCs

Equal amounts of PS-*b*-P2VP and DL-ala (5 mg each) were dissolved in 1 mL of DMF under stirring for 24 h at room temperature. MABr and PdBr$_2$ were added to the polymer solution in a 1 : 1 molar ratio and stirred vigorously overnight to provide sufficient time for the precursor to interact with the P2VP/DL-ala domains. The molar ratio of the 2-vinyl pyridine units in the P2VP block to the perovskite precursors was set as 1 : 1. Afterward, the mixed solution (200 μL) was injected into toluene (5 mL) under vigorous stirring, upon which the PS-*b*-P2VP/DL-ala inverse micelle-encapsulated MAPbBr$_3$ NCs were formed instantaneously in the solution. For further purification, the solution was centrifuged at 10 000 rpm for 5 min using toluene as a solvent and hexane as a precipitant. The volume ratio of *n*-hexane to toluene was 2 : 1. After discarding the supernatant, the precipitate was dispersed in toluene.

Synthesis of OA and OAm-cocapped MAPbBr$_3$ NCs

The MAPbBr$_3$ NCs cocapped with OA and OAm were synthesized according to a typical ligand-assisted reprecipitation process.[24,46] OA (0.5 mL), OAm (20 μL), MABr (0.16 mmol), and PbBr$_2$ (0.2 mmol) were dissolved in 5 mL of DMF, and then, 200 μL of the precursor solution was quickly injected into 5 mL of toluene which acted as a poor solvent under vigorous stirring. Small-molecule ligand capped MAPbBr$_3$ NCs were formed immediately with rapid stirring. No additional purification step was performed to maintain the colloidal stability of the prepared NC solution.

Synthesis of the PS-*b*-P2VP inverse micelle-encapsulated (DL-ala)PbBr$_3$ NCs

First, (DL-ala)Br was prepared in accordance with the procedure reported in the literature.[54,55] DL-ala (1.2 mmol) and HBr (1.3 mmol) were added to 0.5 mL of ethyl alcohol. After vigorous stirring for 2 h, the solution was completely evaporated to obtain a solid precipitate, (DL-ala)Br. Next, (DL-ala)Br (1.5 mg) and PdBr$_2$ (3.4 mg) were added to PS-*b*-P2VP dissolved in DMF and stirred vigorously for 24 h at room temperature, followed by the injection of the precursor solution (200 μL) into toluene (5 mL). Finally, the same purification process was performed.

Characterization

The absorption and PL spectra were obtained using Cary 5000 (Varian) and FP-8500 (JASCO) spectrometers, respectively. The TEM measurements were carried out using a JEM-2100Plus system (JEOL). The FTIR spectra were recorded on an INVENIO-R FTIR spectrometer (Bruker) with a resolution of 1 cm^{-1}, using the KBr pellet technique, and the XRD pattern was obtained using a SPIN-1200D X-ray diffractometer (EPLEX). The CD spectra were recorded on a JASCO J-1500 CD spectrometer. The CPL measurements were carried out with a JASCO CPL-300 spectrophotometer at room temperature. The TRPL data were collected using either a picosecond 440 nm pulsed diode laser (LDH-P-C-440M, PicoQuant) or a femtosecond Yb:KGW

12882 | *J. Mater. Chem. A*, 2023, **11**, 12876–12884

This journal is © The Royal Society of Chemistry 2023

amplifier laser (PHAROS, Light Conversion) and a 10 mm × 10 mm beam-path quartz optical cell, using a home-built time-resolved single photon counting system, a TCSPC board (SPC-130-EMN, Becker-Hickl GmbH), and a silicon-APD detector (ID-100, ID Quantique), interfaced with a monochromator (CM110, Spectral-Products). These measurements were performed at the National Research Facilities and Equipment Center (NanoBio-Energy Materials Center) in Ewha Womans University. In front of the monochromator entrance slit, the 440 nm excitation beam was blocked by a 455 nm long-pass color glass filter. The excitation and emission polarizations were set to a magic angle (54.7°) for all the TRPL experiments. The pulse energy of the excitation beam was controlled by a graduated neutral-density filter and maintained at values less than 10 pJ.

Author contributions

M. K. conceived the concrete idea, performed main experiments, analyzed data, and wrote the manuscript. J. K. performed the CD and XRD measurements. J. B. conducted the TRPL investigation. Y. J. J. edited and reviewed the manuscript. J. P. guided the TRPL investigation and contributed to the interpretation. D. H. K. performed conceptualization, supervision, funding acquisition, project administration, and writing – review & editing.

Conflicts of interest

There are no conflicts to declare.

Acknowledgements

Notes and references

1 J. Ma, H. Wang and D. Li, *Adv. Mater.*, 2021, **33**, 2008785.
2 S. Ma, J. Ahn and J. Moon, *Adv. Mater.*, 2021, **33**, 2005760.
3 C. Ye, J. Jiang, S. Zou, W. Mi and Y. Xiao, *J. Am. Chem. Soc.*, 2022, **144**, 9707–9714.
4 H. Liu, B. Zhang, T. Gao, X. Wu, F. Cui and W. Xu, *Nanoscale*, 2019, **11**, 5506–5511.
5 J. Ma, C. Fang, C. Chen, L. Jin, J. Wang, S. Wang, J. Tang and D. Li, *ACS Nano*, 2019, **13**, 3659–3665.
6 D. Di Nuzzo, L. Cui, J. L. Greenfield, B. Zhao, R. H. Friend and S. C. Meskers, *ACS Nano*, 2020, **14**, 7610–7616.
7 W. Chen, S. Zhang, M. Zhou, T. Zhao, X. Qin, X. Liu, M. Liu and P. Duan, *J. Phys. Chem. Lett.*, 2019, **10**, 3290–3295.
8 Y.-H. Kim, Y. Zhai, E. A. Gaulding, S. N. Habisreutinger, T. Moot, B. A. Rosales, H. Lu, A. Hazarika, R. Brunecky, L. M. Wheeler, J. J. Berry, M. C. Beard and J. M. Luther, *ACS Nano*, 2020, **14**, 8816–8825.
9 Y. Shi, P. Duan, S. Huo, Y. Li and M. Liu, *Adv. Mater.*, 2018, **30**, 1705011.
10 W. Li, M. Xu, C. Ma, Y. Liu, J. Zhou, Z. Chen, Y. Wang, H. Yu, J. Li and S. Liu, *ACS Appl. Mater. Interfaces*, 2019, **11**, 23512–23519.
11 G. H. Debnath, Z. N. Georgieva, B. P. Bloom, S. Tan and D. H. Waldeck, *Nanoscale*, 2021, **13**, 15248–15256.
12 S. Jiang, Y. Song, H. Kang, B. Li, K. Yang, G. Xing, Y. Yu, S. Li, P. Zhao and T. Zhang, *ACS Appl. Mater. Interfaces*, 2022, **14**, 3385–3394.
13 S. Liang, M. Zhang, G. M. Biesold, W. Choi, Y. He, Z. Li, D. Shen and Z. Lin, *Adv. Mater.*, 2021, **33**, 2005888.
14 S. Hou, Y. Guo, Y. Tang and Q. Quan, *ACS Appl. Mater. Interfaces*, 2017, **9**, 18417–18422.
15 H. Han, B. Jeong, T. H. Park, W. Cha, S. M. Cho, Y. Kim, H. H. Kim, D. Kim, D. Y. Ryu, W. K. Choi and C. Park, *Adv. Funct. Mater.*, 2019, **29**, 1808193.
16 V. A. Hintermayr, C. Lampe, M. Löw, J. Roemer, W. Vanderlinden, M. Gramlich, A. X. Böhm, C. Sattler, B. Nickel, T. Lohmüller and A. S. Urban, *Nano Lett.*, 2019, **19**, 4928–4933.
17 B. Zhao, X. Gao, K. Pan and J. Deng, *ACS Nano*, 2021, **15**, 7463–7471.
18 S. Liu, X. Liu, Y. Wu, D. Zhang, Y. Wu, H. Tian, Z. Zheng and W.-H. Zhu, *Matter*, 2022, **5**, 2319–2333.
19 L. Yan, M. K. Jana, P. C. Sercel, D. B. Mitzi and W. You, *J. Am. Chem. Soc.*, 2021, **143**, 18114–18120.
20 A. Hubley, A. Bensalah-Ledoux, B. Baguenard, S. Guy, B. Abécassis and B. Mahler, *Adv. Opt. Mater.*, 2022, **10**, 2200394.
21 M. Liu, L. Zhang and T. Wang, *Chem. Rev.*, 2015, **115**, 7304–7397.
22 X. Li, Y. Wu, S. Zhang, B. Cai, Y. Gu, J. Song and H. Zeng, *Adv. Funct. Mater.*, 2016, **26**, 2435–2445.
23 S. Yang, F. Zhang, J. Tai, Y. Li, Y. Yang, H. Wang, J. Zhang, Z. Xie, B. Xu, H. Zhong, K. Liu and B. Yang, *Nanoscale*, 2018, **10**, 5820–5826.
24 Y. He, Y. J. Yoon, Y. W. Harn, G. V. Biesold-McGee, S. Liang, C. H. Lin, V. V. Tsukruk, N. Thadhani, Z. Kang and Z. Lin, *Sci. Adv.*, 2019, **5**, eaax4424.
25 T. Fukuyama, K. Matsuo and K. Gekko, *J. Phys. Chem. A*, 2005, **109**, 6928–6933.
26 M. Hernández-Orta, E. Pérez, L. E. Cruz-Barba and M. A. Sánchez-Castillo, *J. Mater. Sci.*, 2018, **53**, 8766–8785.
27 L.-C. Chen, Y.-C. Mao, S.-C. Lin, M.-C. Li, R.-M. Ho and J.-C. Tsai, *Chem. Commun.*, 2012, **48**, 3668–3670.
28 T. Wen, H. Y. Shen, H. F. Wang, Y. C. Mao, W. T. Chuang, J. C. Tsai and R. M. Ho, *Angew. Chem., Int. Ed.*, 2015, **54**, 14313–14316.
29 J. Joseph and E. D. Jemmis, *J. Am. Chem. Soc.*, 2007, **129**, 4620–4632.

This journal is © The Royal Society of Chemistry 2023

J. Mater. Chem. A, 2023, **11**, 12876–12884 | **12883**

30 Q. Zhang, H. Fan, L. Zhang and Z. Jin, *Macromolecules*, 2020, **53**, 7025–7033.

31 C.-C. Yang, P. Puneet, I.-M. Lin, Y.-W. Chiang and R.-M. Ho, *Giant*, 2021, **7**, 100059.

32 A. R. Garcia, R. B. de Barros, J. o. P. Lourenco and L. M. Ilharco, *J. Phys. Chem. A*, 2008, **112**, 8280–8287.

33 J. L. Velada, L. C. Cesteros and I. Katime, *Appl. Spectrosc.*, 1996, **50**, 893–899.

34 L. Zuo, H. Guo, D. W. deQuilettes, S. Jariwala, N. De Marco, S. Dong, R. DeBlock, D. S. Ginger, B. Dunn, M. Wang and Y. Yang, *Sci. Adv.*, 2017, **3**, e1700106.

35 S. Förster and M. Antonietti, *Adv. Mater.*, 1998, **10**, 195–217.

36 J. H. Kim, Y. R. Kim, B. Park, S. Hong, I. W. Hwang, J. Kim, S. Kwon, G. Kim, H. Kim and K. Lee, *Small*, 2021, **17**, 2005608.

37 D. M. Jang, K. Park, D. H. Kim, J. Park, F. Shojaei, H. S. Kang, J.-P. Ahn, J. W. Lee and J. K. Song, *Nano Lett.*, 2015, **15**, 5191–5199.

38 S. Chen, Y. Zhang, X. Zhang, J. Zhao, Z. Zhao, X. Su, Z. Hua, J. Zhang, J. Cao, J. Feng, X. Wang, X. Li, J. Qi, J. Li and P. Gao, *Adv. Mater.*, 2020, **32**, 2001107.

39 Y.-C. Shih, Y. B. Lan, C. S. Li, H. C. Hsieh, L. Wang, C. I. Wu and K. F. Lin, *Small*, 2017, **13**, 1604305.

40 J. Du, L. Feng, X. Guo, X. Huang, Z. Lin, J. Su, Z. Hu, J. Zhang, J. Chang and Y. Hao, *J. Power Sources*, 2020, **455**, 227974.

41 I. Ilisz, R. Berkecz and A. Péter, *J. Pharm. Biomed. Anal.*, 2008, **47**, 1–15.

42 Y. J. Yoon, Y. Chang, S. Zhang, M. Zhang, S. Pan, Y. He, C. H. Lin, S. Yu, Y. Chen, Z. Wang, Y. Ding, J. Jung, N. Thadhani, V. V. Tsukruk, Z. Kang and Z. Lin, *Adv. Mater.*, 2019, **31**, 1901602.

43 Z. Wu, M. Jiang, Z. Liu, A. Jamshaid, L. K. Ono and Y. Qi, *Adv. Energy Mater.*, 2020, **10**, 1903696.

44 V. S. Chirvony and J. P. Martínez-Pastor, *J. Phys. Chem. Lett.*, 2018, **9**, 4955–4962.

45 C. Zhao, J. Dai, C. Zhu, X. Liu, H. Dong, F. Yuan, B. Jiao, Y. Yu and Z. Wu, *ACS Appl. Mater. Interfaces*, 2022, **14**, 10508–10516.

46 H. Huang, J. Raith, S. V. Kershaw, S. Kalytchuk, O. Tomanec, L. Jing, A. S. Susha, R. Zboril and A. L. Rogach, *Nat. Commun.*, 2017, **8**, 996.

47 S. Wang, L. Zhou, F. Huang, Y. Xin, P. Jin, Q. Ma, Q. Pang, Y. Chen and J. Z. Zhang, *J. Mater. Chem. C*, 2018, **6**, 10994–11001.

48 V. Y. Sirenko, O. I. Kucheriv, D. D. Naumova, I. V. Fesych, R. P. Linnik, I.-A. Dascălu, S. Shova, I. O. Fritsky and A. Il'ya, *New J. Chem.*, 2021, **45**, 12606–12612.

49 A. Jancik Prochazkova, S. Demchyshyn, C. Yumusak, J. Masilko, O. Bruggemann, M. Weiter, M. Kaltenbrunner, N. S. Sariciftci, J. Krajcovic, Y. Salinas and A. Kovalenko, *ACS Appl. Nano Mater.*, 2019, **2**, 4267–4274.

50 A. K. Sharma, P. Bansal, G. K. Nim and P. Kar, *Part. Part. Syst. Charact.*, 2019, **36**, 1900328.

51 M. K. Jana, R. Song, H. Liu, D. R. Khanal, S. M. Janke, R. Zhao, C. Liu, Z. Valy Vardeny, V. Blum and D. B. Mitzi, *Nat. Commun.*, 2020, **11**, 4699.

52 Y. H. Kim, R. Song, J. Hao, Y. Zhai, L. Yan, T. Moot, A. F. Palmstrom, R. Brunecky, W. You, J. J. Berry, J. L. Blackburn, M. C. Beard, V. Blum and J. M. Luther, *Adv. Funct. Mater.*, 2022, **32**, 2200454.

53 D. Yang, X. Li and H. Zeng, *Adv. Mater. Interfaces*, 2018, **5**, 1701662.

54 J. Ahn, S. Ma, J.-Y. Kim, J. Kyhm, W. Yang, J. A. Lim, N. A. Kotov and J. Moon, *J. Am. Chem. Soc.*, 2020, **142**, 4206–4212.

55 A. Ishii and T. Miyasaka, *Sci. Adv.*, 2020, **6**, eabd3274.

12884 | *J. Mater. Chem. A*, 2023, **11**, 12876–12884

This journal is © The Royal Society of Chemistry 2023